Cell Reports
Physical Science

CellPress
OPEN ACCESS

Article

Topology and ground state control in open-shell donor-acceptor conjugated polymers

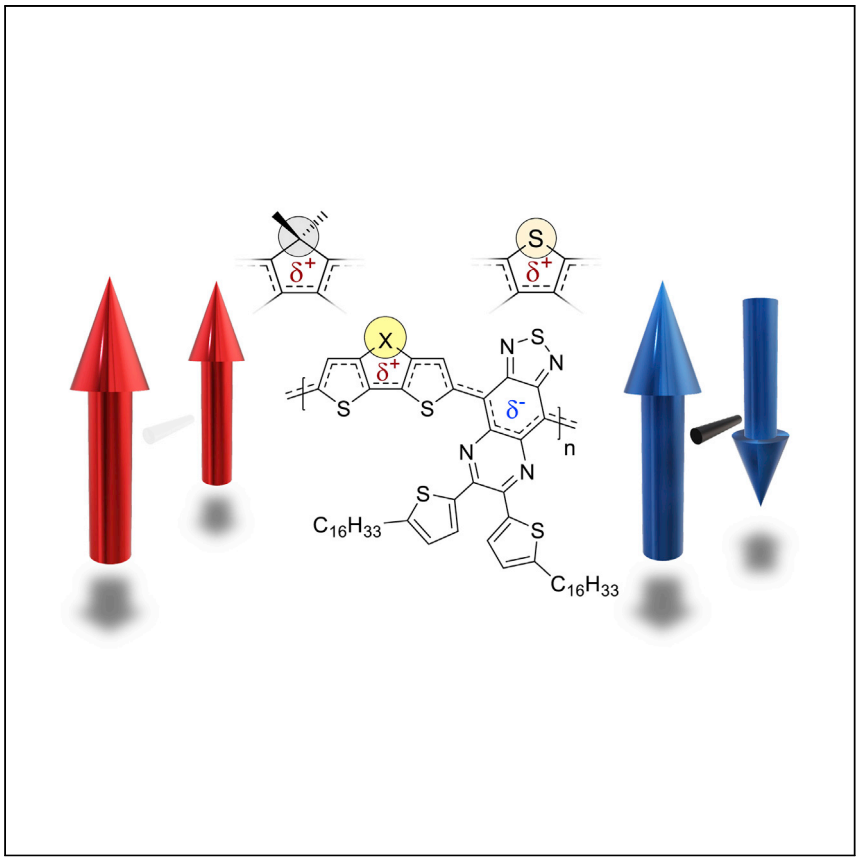

Donor-acceptor (DA) conjugated polymers (CPs) with narrow bandgaps and open-shell (diradical) character demonstrate emergent phenomena that emanate from their collective electronic properties and diminished electron pairing. Mayer et al. report DA CPs that enable a strategy to control the ground state spin multiplicity and connect structural, physicochemical, electronic, spin, and magnetic properties.

Kevin S. Mayer, Daniel J. Adams, Naresh Eedugurala, ..., Xiaodan Gu, Michael K. Bowman, Jason D. Azoulay

jason.azoulay@usm.edu

Highlights

Synthesis of low-spin and high-spin donor-acceptor conjugated polymers

Connections linking structural, physicochemical, electronic, and magnetic properties

Open-shell donor-acceptor conjugated polymers with novel properties

Mayer et al., Cell Reports Physical Science 2, 100467
June 23, 2021
https://doi.org/10.1016/j.xcrp.2021.100467

Cell Reports
Physical Science

CellPress
OPEN ACCESS

Article

Topology and ground state control in open-shell donor-acceptor conjugated polymers

Kevin S. Mayer,[1] Daniel J. Adams,[1] Naresh Eedugurala,[1] Molly M. Lockart,[2] Paramasivam Mahalingavelar,[1] Lifeng Huang,[1] Luke A. Galuska,[1] Eric R. King,[1] Xiaodan Gu,[1] Michael K. Bowman,[2] and Jason D. Azoulay[1,3,4,*]

SUMMARY

Donor-acceptor (DA) conjugated polymers (CPs) with narrow bandgaps and open-shell (diradical) character represent an emerging class of materials whose rich behavior emanates from their collective electronic properties and diminished electron pairing. However, the structural and electronic heterogeneities that define these materials complicate bandgap control at low energies and connections linking topology, exchange interactions, and (opto) electronic functionality remain nascent. To address these challenges, we demonstrate structurally rigid and strongly π-conjugated copolymers comprised of a solubilizing thiadiazoloquinoxaline acceptor and cyclopenta[2,1-*b*:3,4-*b*′]dithiophene or dithieno [3,2-*b*:2′,3′-*d*]thiophene donors. Atom-specific substitution modulates local aromatic character within the donor resulting in dramatic differences in structural, physicochemical, electronic, and magnetic properties of the polymers. These long-range π-mediated interactions facilitate control between low-spin aromatic and high-spin quinoidal forms. This work provides a strategy to understand the evolution of the electronic structure within DA CPs, control the ground state spin multiplicity, tune spin-spin interactions, and articulate the emergence of their novel properties.

INTRODUCTION

Organic semiconductors (OSCs) with open-shell electronic structures offer a rich materials space for accessing new properties derived from unpaired electrons coupled to light elements and the utilization of diverse spin-correlated phenomena that can be tuned through chemical syntheses.[1-4] These materials have enabled fundamental insight into the nature of π-bonding and electron pairing, the creation of novel (opto)electronic functionalities, and offered materials relevant in emerging technologies such as molecular and organic electronics,[2-6] non-linear optics,[7] singlet fission,[8,9] energy conversion and storage,[10-12] spintronics,[13,14] and quantum information.[15,16] Diverse classes of materials have been demonstrated including polycyclic aromatic hydrocarbons (PAHs) and related structures,[3,17-19] open-shell graphene fragments,[20] zigzag edge graphene nanoribbons (ZGNRs),[3,18,21-25] quinoidal oligothiophenes,[26,27] and conjugated polymers (CPs) (Figures 1A–1C).[31-35] These materials share common characteristics including degenerate or near-degenerate frontier molecular orbitals (MOs), weak intramolecular electron-electron pairing, efficient spin polarization throughout the π-conjugated structure, and a considerable narrowing of the energy gap between spin states. This results in richer categories of behavior and distinct optical, excited

[1]Center for Optoelectronic Materials and Devices, School of Polymer Science and Engineering, The University of Southern Mississippi, Hattiesburg, MS 39406, USA

[2]Department of Chemistry & Biochemistry, The University of Alabama, Tuscaloosa, AL 35487-0336, USA

[3]Twitter: @AzoulayGroup

[4]Lead contact

*Correspondence: jason.azoulay@usm.edu

https://doi.org/10.1016/j.xcrp.2021.100467

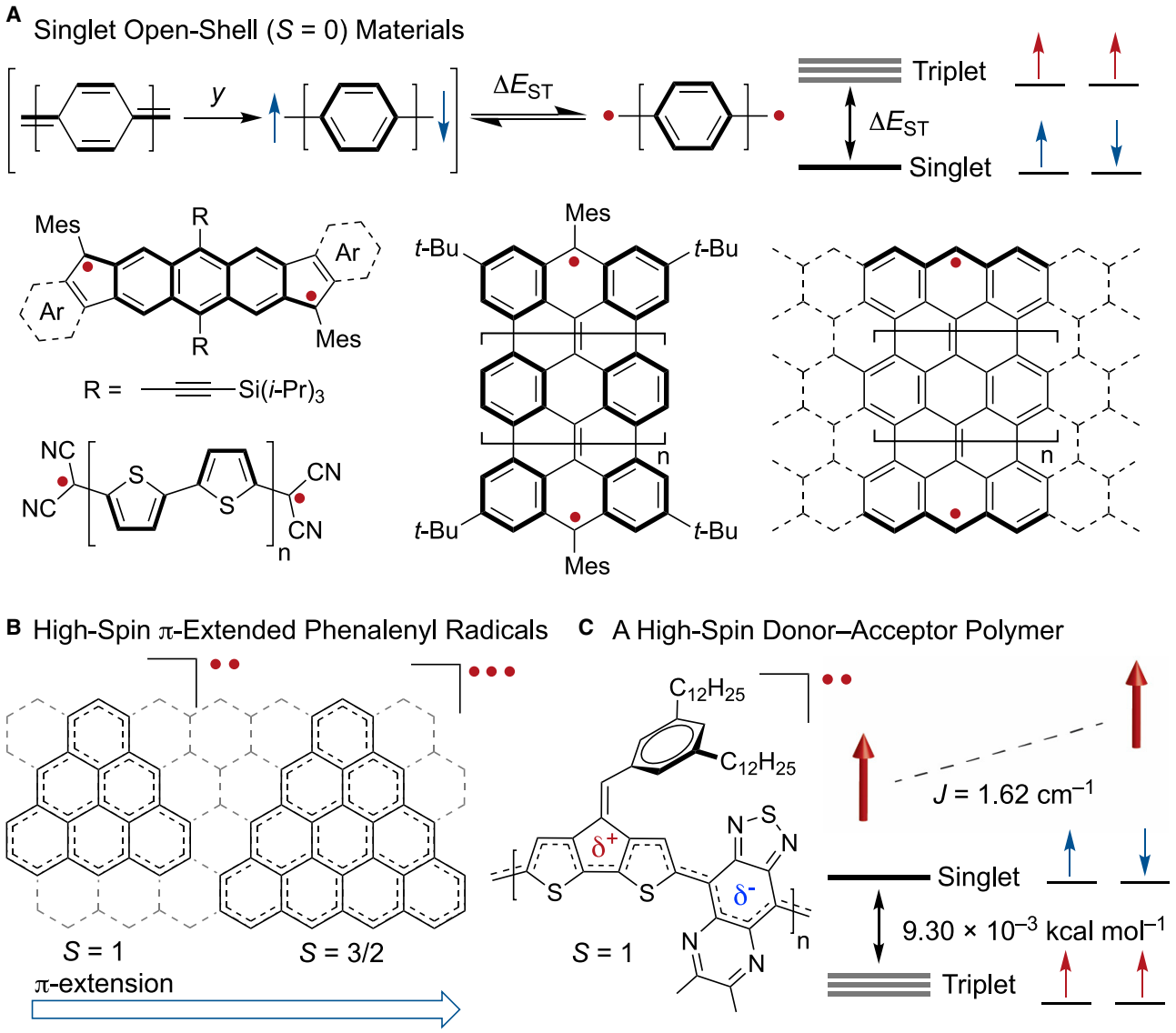

Figure 1. Molecules and polymers with delocalized electronic structures and open-shell ground states

(A) Electronic structure of open-shell Kékulé diradicals described by the diradical character index (*y*), which illustrates the resonance between closed- and open-shell structures and the energy difference between the singlet ground state and thermally populated triplet state, ΔE_{ST}. Diindenoanthracenes,[28] quinoidal oligothiophene framework,[29] anthenes,[30] and ZGNRs[18] drawn in their open-shell resonance forms (Ar, fused aryl group; Mes, 2,4,6-trimethylphenyl).

(B) Representative examples of π-extended systems that exhibit high-spin ground states and extensive spin-polarization synthesized using ultrahigh vacuum conditions.[20]

(C) Conjugated DA copolymer with a high-spin ground state and a high-to-low-spin energy gap of 9.30 × 10^{-3} kcal mol^{-1}.[31]

state, electronic, spin, and magnetic properties not available from their closed-shell counterparts.

The diradical character index (*y*) represents the degree of electron correlation or the effective bond order. This index ranges from $0 < y < 1$ and correlates with physicochemical properties and (opto)electronic functionality.[3,4,7,24,31,36] Synthetic and characterization efforts have capitalized on the discrete nature of well-defined molecular systems resulting in the elucidation of chemical, structural, and topological

features that promote diradical character. Design strategies for delocalized Kekulé diradicals generally include: (1) embedding quinoidal (pro-aromatic) structures within π-frameworks whereby aromaticity recovery diminishes the covalency of a π-bond and results in adaptation of an open-shell ground state; (2) topologies that promote the spatial distribution of frontier MOs; and (3) a narrowing of the bandgap that results in configurational admixing (Figures 1A–1C).[3,4,23,25,31,37,38] The unifying features of these materials are structures that resemble a resonance hybrid of closed- and open-shell forms with a singlet ground state (spin quantum number, $S = 0$) and a singlet-triplet gap (ΔE_{ST}) that allows for thermal population of a high-spin state ($S \geq 1$) with spin interactions between π electrons (Figure 1A).[3,25,26,39] Prototypical non-Kekulé molecules form the basis for high-spin materials.[20,40,41] These are predominately synthesized using photochemical or redox reactions on molecular precursors with prearranged topologies. This approach results in half-occupied degenerate MOs that exhibit strong exchange mediated via orbitals in close spatial proximity.[40] While materials with very high-spin quantum numbers and emergent spin and magnetic properties have been achieved, nearly all are unstable, highly localized, and offer limited flexibility in molecular design.[40,42-44] These well-defined Kekulé and non-Kekulé materials have enabled important correlations between electronic structure, spin-spin coupling, exchange, and intermolecular interactions in emerging functional materials. A nascent challenge exists for larger open-shell π-systems, whose properties develop as a result of their collective electronic properties and emanate from spin-spin coupling over longer distances than in other open-shell materials. Pioneering efforts have demonstrated atomically precise surface-mediated syntheses of open-shell molecules such as polynuclear benzenoid species, nanographenes,[20,45] ZGNRs,[21,22,46] and polymers under ultrahigh vacuum conditions (Figures 1A and 1B).[47,48] This has enabled clear correlations between topological, spin, and magnetic structures with physical observables. However, the intrinsic instability of these materials precludes bottom-up "wet-chemical" approaches, limiting practical utilization within thin-film, nanostructured, and solution-processed technologies.

Donor-acceptor (DA) CPs define a family of materials with exceptional electronic properties and find broad utility in (opto)electronic technologies as a result of their strong interactions with light, diverse transport phenomena, chemical stability, and properties that can be tuned using chemical synthesis.[49,50] While most CPs are closed-shell species accommodating their π electrons in bonding orbitals, several reports have demonstrated that DA copolymers with embedded quinoidal subunits, extensive delocalization, and very narrow bandgaps show diradical character.[31-34,51,52] We previously demonstrated that charge-neutral cyclopentadithiophene-thiadiazoloquinoxaline (CPDT-TQ) copolymers can adopt high-spin ground states (Figure 1C).[31,33] Several attributes of these materials are noteworthy and offer properties that are otherwise difficult to achieve in other open-shell systems. In these DA CPs, a high degree of electronic coherence along the π-conjugated backbone leads to a narrowing of the bandgap and increased configurational admixing. The extended π-system enables topological localization of α- and β-singly occupied MOs (SOMOs) to opposite sides of the macromolecule, diminishing the covalency of the ground state and increasing y. Stable, high-spin ($S = 1$) ground states are achieved as a result of long-range π-mediated spin-spin interactions.[31] This contrasts with both prototypical non-Kekulé species where strong exchange and ferromagnetic coupling is mediated through bonds in close proximity[40] and Kekulé materials where dynamic spin polarization (DSP) largely results in a singlet ground state with antiferromagnetically coupled spins (Figure 1A).[23,37,53] These species are also distinct from doped CPs in which radical species are formed via ion pair

and ground state charge transfer complex formation.[54] The vast majority of open-shell species are highly unstable owing to their electron-rich nature and localized radical sites. In DA CPs, there is significant internal charge transfer character between electron-rich and electron-deficient units along the π-conjugated backbone resulting in extensive spin-polarization and thermodynamic stability. This picture differs from electron-rich PAHs, nanographenes, or ZGNRs in which SOMOs populate zigzag edges, or π-systems that require kinetic blocking of open-shell sites with sterically bulky substituents that mask important π-π and spin-spin interactions (Figure 1A).[43,55-57]

Approaches to access and tune the properties of open-shell materials with delocalized electronic structures and highly correlated ground states are at the forefront of advancing our fundamental understanding of the relationship between molecular structure, electronic topology, and the achievable properties of these complex materials systems. While DA CPs fill an essential gap, a fundamental knowledge of how to manipulate the underlying properties that influence *y* and various interrelated phenomena remains absent. The chemical, electronic, and structural heterogeneities that affect the degree of correlation and conformational disorder in these materials complicate bandgap control at low energies, the development of design rules that favor open-shell ground states, and the topological modulation of exchange coupling. Furthermore, current state-of-the-art approaches do not adequately account for magnetic interactions, long-range spin-polarization, Coulomb and Pauli repulsion, electrostatics, hyperfine interactions, and higher-order electronic and quantum mechanical correlations that give rise to the properties exhibited by these structurally and energetically heterogeneous extended π-systems.[58]

RESULTS

Synthesis of low- and high-spin open-shell DA CPs

These profound experimental and theoretical challenges motivated our efforts to develop an approach to investigate and understand how properties coalesce in open-shell DA CPs so as to rationally modulate the ground state electronic structure and exchange coupling coefficient (*J*) ($J > 0$, parallel; $J < 0$, anti-parallel). Mechanistic studies of such species and the delineation of key structure-function relationships are aided by structural rigidity, which helps to articulate how factors such as spin-polarization, topology, mechanistic pathways for facilitating exchange, and (opto)electronic properties emerge.[59] Figure 2 displays the copolymers considered in this study. We targeted DA CPs comprised of a solubilizing TQ acceptor with ancillary hexadecylthiophene substituents and 4,4-dimethyl-4*H*-cyclopenta[2,1-*b*:3,4-*b*′]dithiophene (CPDT) or dithieno[3,2-*b*:2′,3′-*d*]thiophene (DTT) donors. The TQ acceptor can impart unique electronic properties to π-conjugated systems such as a narrow bandgap, high electron affinity, and a tendency to favor quinoidal bonding patterns[60,61]—features that form and stabilize unpaired spins within DA CPs.[31,33] This particular framework promotes linear backbones that support long-range π-conjugation and transmission of spin information necessary to compare atom-specific and subtle effects that influence the properties of the materials.

Our synthetic approach is shown in Figure 2 and begins with the preparation of 1,2-bis(5-hexadecylthiophen-2-yl)ethane-1,2-dione (**1**). Linear ($-C_{16}H_{33}$) solubilizing groups were chosen on the basis of minimizing torsion and promoting sufficient solubility of the polymer products. The reaction between 2-hexadecylthiophene and oxalyl chloride was carried out using a Friedel-Crafts acylation in the presence of aluminum trichloride ($AlCl_3$), providing the diketone in 88% yield (Figures 2A and S1). The condensation

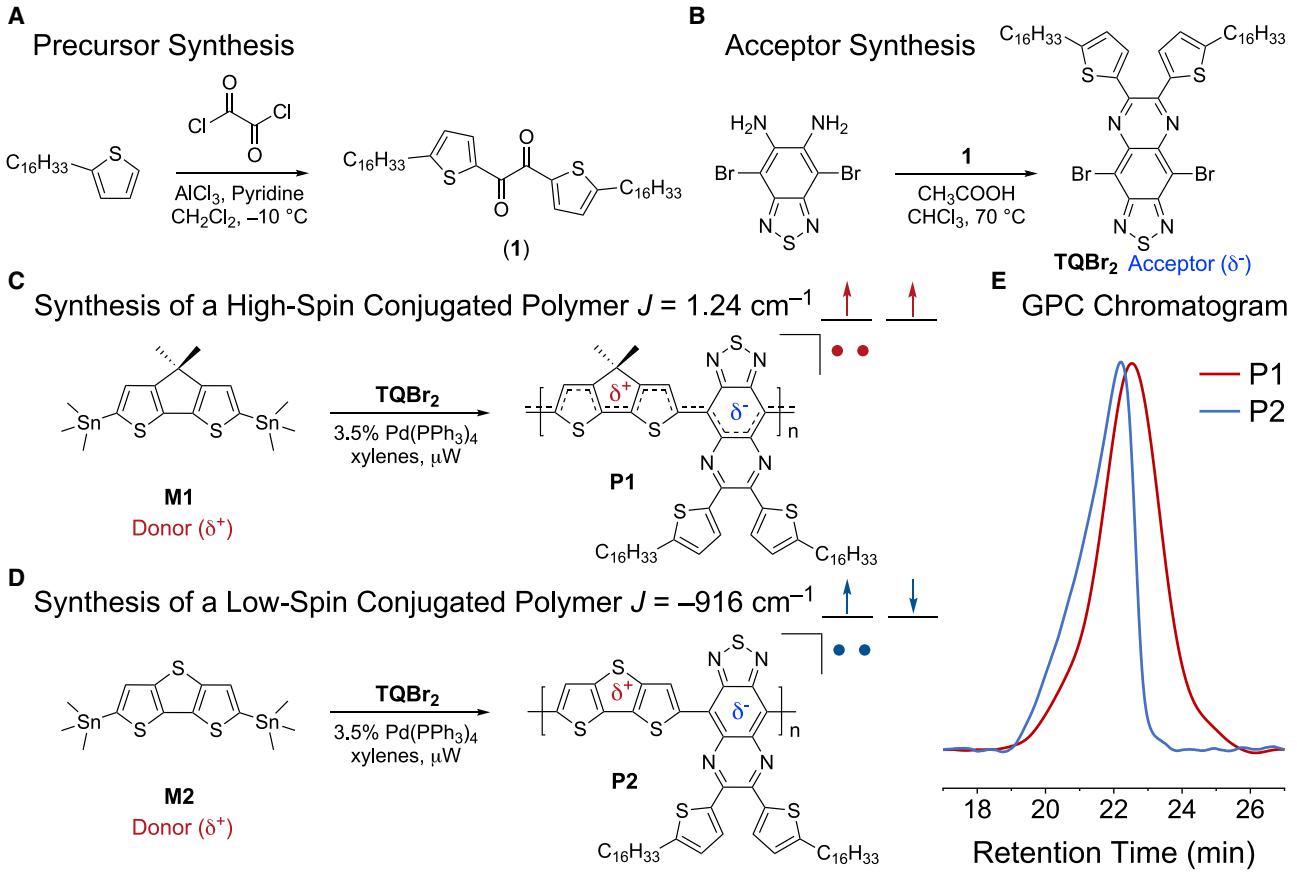

Figure 2. Synthesis of high- and low-spin DA CPs using a Stille cross-coupling copolymerization

(A) Synthesis of 1,2-bis(5-hexadecylthiophen-2-yl)ethane-1,2-dione (**1**): –10°C (20 min) to r.t.

(B) Synthesis of $TQBr_2$: 70°C (5 days).

(C) The rapid polymerization approach used to synthesize the high-spin polymer **P1** using a microwave-mediated Stille cross-coupling copolymerization between (4,4-dimethyl-4*H*-cyclopenta[2,1-*b*:3,4-*b*′]dithiophene-2,6-diyl)bis(trimethylstannane) (**M1**) and $TQBr_2$. Conditions: 120°C (5 min), 140°C (5 min), 170°C (30 min).

(D) Synthesis of low-spin **P2** using a microwave-mediated Stille cross-coupling copolymerization between 2,6-bis(trimethylstannyl)dithieno[3,2-*b*:2′,3′-*d*]thiophene (**M2**) and $TQBr_2$. Conditions: 120°C (5 min), 140°C (5 min), 170°C (45 min).

(E) GPC traces of **P1** and **P2** obtained at 160°C in 1,2,4-trichlorobenzene.

between **1** and 4,7-dibromobenzo[*c*][1,2,5]thiadiazole-5,6-diamine[62] was carried out in an acetic acid:chloroform mixture (5:1) providing 4,9-dibromo-6,7-bis(5-hexadecylthiophen-2-yl)-[1,2,5]thiadiazolo[3,4-*g*]quinoxaline ($TQBr_2$) in 35% yield (Figures 2B and S2).[63] The donors (4,4-dimethyl-4*H*-cyclopenta[2,1-*b*:3,4-*b*′]dithiophene-2,6-diyl)bis(trimethylstannane) (**M1**) and 2,6-bis(trimethylstannyl)-dithieno[3,2-*b*:2′,3′-*d*]thiophene (**M2**) were prepared according to literature procedures.[64,65] As shown in Figure 2, the microwave-assisted Stille cross-coupling copolymerizations were carried out between **M1** and **M2** with $TQBr_2$, producing poly(4-(4,4-dimethyl-4*H*-cyclopenta[2,1-*b*:3,4-*b*′]dithiophen-2-yl)-6,7-bis(5-hexadecylthiophen-2-yl)-[1,2,5]thiadiazolo[3,4-*g*]quinoxaline) (**P1**, Figures 2C and S3) and poly(4-(dithieno[3,2-*b*:2′,3′-*d*]thiophen-2-yl)-6,7-bis(5-hexadecylthiophen-2-yl)-[1,2,5]thiadiazolo[3,4-*g*]quinoxaline) (**P2**, Figures 2D and S3), respectively.[31] The utilization of $Pd(PPh_3)_4$ as the catalyst in xylenes resulted in soluble copolymers following purification via Soxhlet extraction. Gel permeation chromatography (GPC) at 160°C in 1,2,4-trichlorobenzene showed number average molar masses (M_n) of 14.2 and 30.5 kg mol^{-1} and dispersities ($Đ$) of 2.24 and 1.91 for **P1** and **P2**, respectively (Figure 2E).

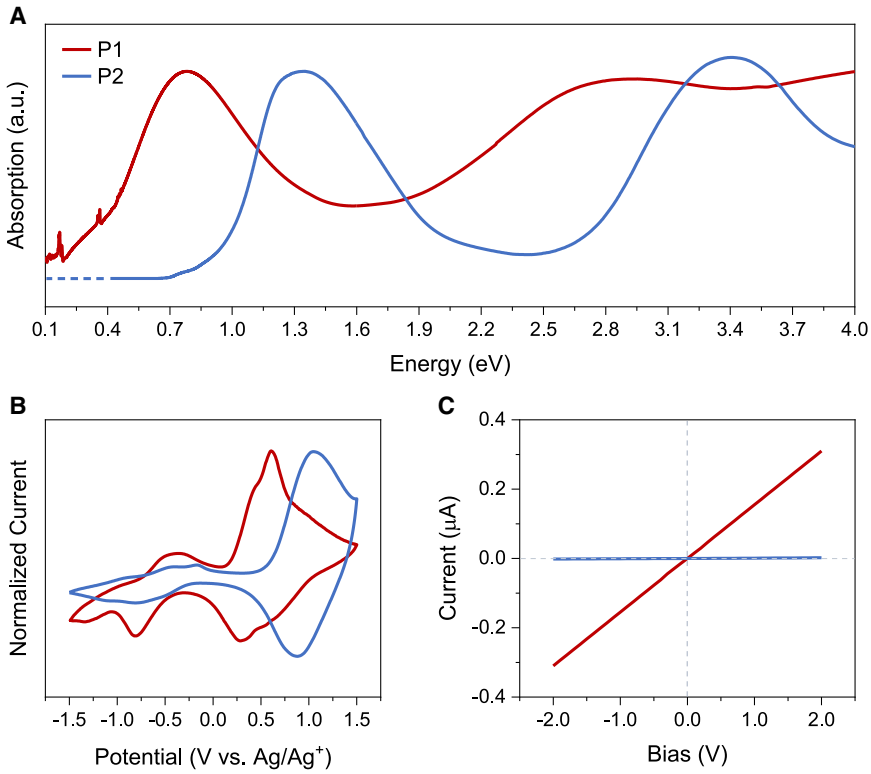

Figure 3. Solid-state properties of polymer thin films

(A) Absorption spectra of **P1** and **P2** thin films cast from chlorobenzene onto an NaCl substrate.
(B) Cyclic voltammetry indicates a HOMO-LUMO energy gap of 0.38 and 0.76 eV for **P1** and **P2**.
(C) Current-voltage characteristics in a 30 μm × 1 mm channel with σ_{RT} of 6.75 × 10^{-4} and 7.46 × 10^{-6} S cm^{-1} for **P1** and **P2**.

The solubility of **P1** and **P2** enabled solution processing; thus, thin films were prepared by spin coating 10 mg mL^{-1} chlorobenzene solutions of the polymers onto NaCl substrates. **P1** displays a broad absorption profile with an absorption maximum (λ_{max}) centered at 1.68 μm and a band-tail extending throughout the infrared in which vibrational features are superimposed (Figures 3A and S4). The optical bandgap (E_g^{opt}) is less than 0.10 eV, as estimated from the thin film absorption onset, comparatively lower than previously reported CPDT-TQ copolymers.[31,33] This can be attributed to the ancillary thiophene substituents that raise the highest occupied molecular orbital (HOMO) and minimize torsion through strategic positioning of solubilizing $-C_{16}H_{33}$ substituents when paired with **M1**. The extensive π-conjugation and high degree of electronic coherence is evident from an E_g^{opt} that is among the lowest obtained for conjugated organic materials and lower than the longest porphyrin arrays (E_g^{opt} = 0.18 eV) that require covalent fusion of the π-conjugated backbone to overcome conjugation saturation behavior.[66] The effect of heteroatom substitution indicates a significant perturbation to the electronic and optical properties. **P2** demonstrates a λ_{max} of 1.29 μm with an absorption onset at 1.80 μm giving E_g^{opt} = 0.69 eV. Cyclic voltammetry (CV) shows that the HOMO of **P1** is located at –4.41 eV and the lowest unoccupied molecular orbital (LUMO) at –4.03 eV, which gives an electrochemical bandgap (E_g^{elec}) of 0.38 eV (Figure 3B). The electrochemical characteristics of **P2** show E_{HOMO} = –4.86 eV, E_{LUMO} = –4.10 eV, and E_g^{elec} of 0.76 eV.

The transport properties of the polymers were evaluated using bottom gate, bottom contact field-effect transistors (FETs). Active layers were deposited by spin-coating chlorobenzene solutions (10 mg mL^{-1} polymer) onto pre-patterned Si/SiO_2

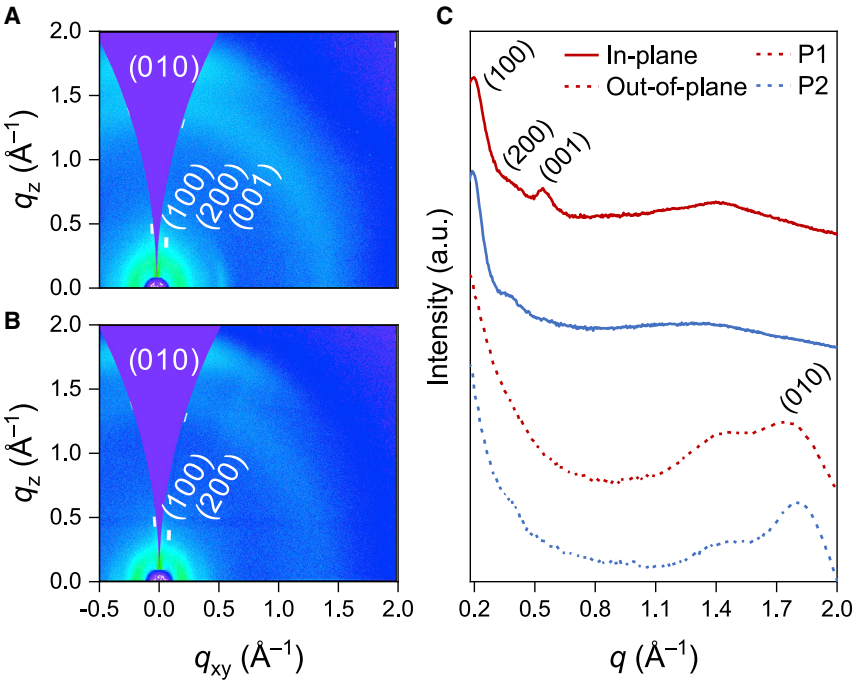

Figure 4. GIWAXS measurements of polymer thin films

(A and B) Two-dimensional GIWAXS profiles of (A) **P1** and (B) **P2**.

(C) One-dimensional line cuts of the integrated in-plane and out-of-plane GIWAXS profiles illustrating distinct backbone packing in **P1**, π-π stacking, and weakly ordered lamellar stacking for both **P1** and **P2**.

(300 nm)/octadecyltrichlorosilane/Au (60 nm) substrates. FET characteristics for **P1** and **P2**, obtained from the transfer and output curves (Figure S5), revealed charge carrier mobilities (μ) of 2.06 × 10^{-4} and 7.19 × 10^{-4} cm^2 V^{-1} s^{-1} and carrier concentrations of 2.05 × 10^{19} and 6.49 × 10^{16} cm^{-3}, respectively. The transfer curves (Figure S5, inset) do not demonstrate any appreciable off state, which is consistent with the presence of free carriers. Thus, Figure 3C highlights the room-temperature conductivities (σ_{RT}) measured without the application of a gate bias. **P1** and **P2** showed linear current-voltage (*I-V*) characteristics with σ_{RT} = 6.75 × 10^{-4} and 7.46 × 10^{-6} S cm^{-1}, respectively. The Ohmic transport in these polymers can be associated with the narrow bandgaps that promote a low energetic barrier for thermal excitation of free carriers and extensive delocalization. The higher σ_{RT} of **P1** correlates with the higher carrier concentration obtained for this material.[33]

Grazing incidence wide-angle X-ray scattering (GIWAXS) profiles for the thermally annealed films are shown in Figure 4. **P1** and **P2** films are weakly crystalline, attributed to the ancillary placement of $-C_{16}H_{33}$ side chains at a site remote from the polymer backbone. The presence of low *q* peaks (~0.19 Å^{-1}, ~33.1 Å) is due to weakly ordered lamellar stacking from $-C_{16}H_{33}$ side chains as indicated from (100) scattering peaks. In addition, **P1** shows additional in-plane (001) peaks at *q* ~0.54 Å^{-1} (*d* ~11.6 Å) and weak (200) peaks at *q* ~0.38 Å^{-1}, which can be attributed to backbone scattering and additional side-chain ordering (Figures 4A and 4C). **P1** and **P2** possess clear out-of-plane peaks at *q* ~1.77 Å^{-1} (*d* ~3.55 Å) and *q* ~1.79 Å^{-1} (*d* ~3.51 Å), respectively, which is attributed to intermolecular ordering due to π-π stacking with a face-on arrangement. Upon thermal annealing of **P2**, a weak (200) in-plane peak became evident (~0.38 Å^{-1}); however, no (001) in-plane peak

emerged (Figures 4B, 4C, and S6). The presence and intensity of the (001) scattering peak in **P1**, compared to **P2**, indicates a more rigid polymer backbone for **P1**.

Electron paramagnetic resonance and magnetic susceptibility measurements

These polymers provide advantages over other open-shell materials and DA CPs for establishing connections between chemical, topological, spin, and magnetic structures with physicochemical properties and (opto)electronic functionality. These include: (1) the facile preparation of copolymers that overcome rapid conjugation saturation behavior and result in extensive delocalization, (2) high chemical stability, (3) neutral open-shell ground states, (4) solubility that enables processing into thin films, and (5) spin-spin coupling and electronic communication dominated by intramolecular through-bond interactions. These collective attributes are difficult to achieve from other materials systems.

The magnetic properties of the polymers were studied using a combination of electron paramagnetic resonance (EPR) spectroscopy and superconducting quantum interference device (SQUID) magnetometry. At room temperature, continuous wave (CW) EPR shows a broad single line 3–7 Gauss wide with a g factor (g) of 2.0035 for **P1**, while **P2** displayed a single line with a lower intensity and increased line width of 5–10 Gauss at $g = 2.0039$ (Figure 5A). The spin concentrations for **P1** and **P2** are 1.31×10^{20} and 4.26×10^{19} spins per gram, respectively. EPR measurements of a dilute solution of **P1** ($\sim 10^{-5}$ M) were used to elucidate the single-chain behavior. The intensity of the signal increased with cooling indicating a paramagnetic ground state (Figures 5B and S7). The variable-temperature (VT) EPR data for **P1** was fit to the Bleaney-Bowers equation in the 5–20 K range, giving $\Delta E_{ST} = 7.10 \times 10^{-3}$ kcal mol^{-1} (Figure 5C).[67] This indicates a high-spin ground state that is nearly degenerate with a thermally accessible low-spin state. The exchange coupling constant $J = 1.24$ cm^{-1} is consistent with weak ferromagnetic coupling ($J > 0$).[1] Magnetic susceptibility (χ) measurements on **P1** via SQUID magnetometry demonstrate a decrease in χ as temperature increased (Figures 5D, S8A, and S8B), consistent with the results obtained by EPR. The magnetization (M) versus applied field (H) plots at 5, 6, and 7 K were fit to the Brillouin function,[31] from which we find $S = 0.99$ (Figure 5D, inset).[68] This result is consistent with **P1** having the high-spin ($S = 1$) ground state of an open-shell diradical.

In contrast, the magnetic susceptibility of **P2** was primarily diamagnetic in the 3 to 150 K range, with a sharp upturn, indicating enhancement in the paramagnetic contribution beginning at approximately 175 K (Figures 5E, 5F, and S8C). Thus, ΔE_{ST} for **P2** was determined through fitting the χT versus T data to the Bleaney-Bowers equation, giving $\Delta E_{ST} = -5.24$ kcal mol^{-1} with $J = -916$ cm^{-1} (Figure 5F).[69] This indicates a low-spin ground state with antiferromagnetic coupling ($J < 0$) and thermal population of a high-spin (triplet) state with ferromagnetic interactions between unpaired π electrons. The literature is replete with examples of room temperature CW-EPR spectra emanating from CPs that are attributed to impurities, doping, polaronic species, etc. However, few reports have considered how these could be diagnostic of different ground state electronic structures. The ΔE_{ST} obtained for **P1** is consistent with ~75% of spins (Boltzmann population ratio of 0.98) occupying the lower energy and triply degenerate high-spin manifold at room temperature. The EPR signal of **P2** is much weaker because only ~0.05% of the polymers are thermally populated triplets under the same conditions.

Insight into the coupling between unpaired electron spins and atomic nuclei along the polymer chain was provided by pulsed EPR of **P1** using the two-pulse electron spin echo envelope modulation (2P-ESEEM) technique (Figure S9).[70,71] Figure 6A

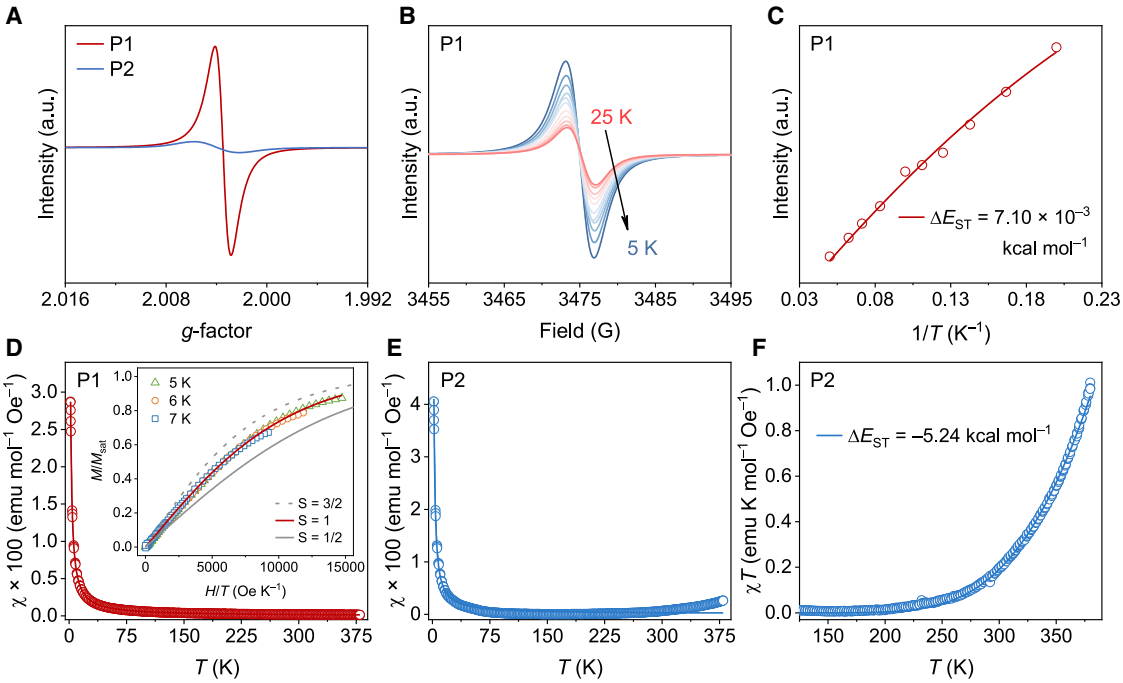

Figure 5. Magnetic properties of the polymers

(A–C) EPR (X-band) spectra (A) of **P1** and **P2** at room temperature and (B) spectra for **P1** from 5 to 25 K with (C) temperature-dependent fit to the Bleaney-Bowers equation with ΔE_{ST} of 7.10 × 10^{-3} kcal mol^{-1}.

(D) SQUID magnetometry of solid sample **P1**. Main plot: Magnetic susceptibility, χ versus T, from 2 to 375 K fit to the Curie-Weiss law (red line). Inset: temperature (T) normalized magnetic field (H) dependence of the magnetization (M) at 5, 6, and 7 K, plotted as M/M_{sat} versus H/T, with Brillouin functions for S = 3/2 (gray dashed line), 1 (red solid line), and 1/2 (gray solid line).

(E) SQUID magnetometry of solid sample **P2** showing magnetic susceptibility, χ versus T, from 2 to 375 K fit to the Curie-Weiss law (blue line).

(F) Observed χT versus T dependence and the temperature-dependent fit to the Bleaney-Bowers equation with ΔE_{ST} of −5.24 kcal mol^{-1}.

shows the spin-echo decay profiles measured with the Hahn echo pulse sequence (π/2-τ-π-τ-echo) at 5 K. The echo decay is modulated by hyperfine interactions between the electron spin and the nuclear spins of the polymer. The overall decay of the spin echo shows that motion of the electron along the chain has relatively low spectral density (decay time <1,000 ns) on the 100–1,000 ns timescale, indicating a relatively long residence time for the spin on a portion of the chain, rather than complete delocalization or rapid thermally activated hopping along or between chains. Fourier-transformed ESEEM spectra are shown in Figure 6B. Dominant peaks centered at 4 MHz and a weaker intensity peak around 15 MHz indicate hyperfine interactions of the electron spin with ^{14}N and ^{1}H, respectively. These hyperfine interactions are static during each spin echo measurement, confirming relatively immobile spins on the polymer. These ESEEM results together with the fairly narrow EPR line width indicate that each unpaired electron spin is confined to but delocalized over roughly 1–3 repeating units.

Quantum chemical calculations

Density functional theory (DFT) calculations at the unrestricted (U)B3LYP/6-31G** level of theory[72] were carried out on oligomers with an increasing number of repeat units (n) in order to understand the evolution of the electronic structure and relate it to the properties of the polymers (Figures S10–S23; Tables S1–S11). The dimer (n = 2) of **P1** adopts a closed-shell ground state (y = 0) with a mixed aromatic-quinoidal bonding pattern resulting from the strong, proquinoidal TQ acceptor (Figure S10; Tables S1 and S8). In progressing from n = 2 → 4, the open-shell

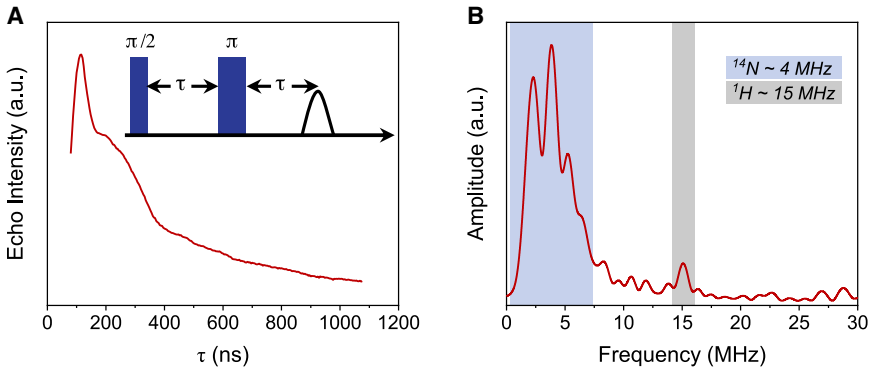

Figure 6. Pulsed EPR spectroscopy measurements of high-spin P1

(A) 2P-ESEEM intensity echo decay of **P1** over time generated with a Hahn echo pulse sequence (inset).

(B) Fourier transformed spectra of powder sample at 5 K and characteristic peaks indicating nuclear hyperfine interactions.

(unrestricted) solution becomes lower in energy and the tetramer (n = 4) exhibits moderate diradical character (y = 0.313). Bond-length alternation (BLA) analysis and nucleus independent chemical shift (NICS) calculations show molecular features associated with an increase of y upon extension of the conjugation length (Figure S10; Tables S2–S11). This includes an increase in the quinoidal character of the oligomer core consistent with NICS values of central TQ benzenoid rings that decrease from –4.44 ppm at n = 4 (ring 13, Table S4) to –1.45 ppm at n = 8 (ring 29, Table S6). This is accompanied by a lengthening of long bonds within these rings from 1.443 Å for n = 4 (bond 21, Table S9) to 1.453 Å for n = 8 (bond 45, Table S11). NICS values of TQ benzenoid rings located at chain ends of the n = 8 oligomer are more aromatic (Figures 7A and 7B; Tables S2–S6). This greater aromatic character is coincident with regions of localized spin density, consistent with a progressive localization of the α- and β-SOMOs to chain ends as shown in Figure 7. The diradical character increases rapidly with oligomer length (y = 0.31 → 0.95 from n = 4 → 8) with a concomitant decrease in the bandgap and ΔE_{ST} to 6.0 × 10^{-3} eV at n = 8 (Table S1; Figures S10, S15, S17, and S20). Extrapolation of these data indicate stabilization of the high-spin ground state at a relatively short chain length of n ~10 (M_n of ~10 kg mol^{-1}).[25,73]

In stark contrast, the substitution of $C(CH_3)_2$ at the donor bridgehead position with the sulfur atom possessing vacant *d*-orbitals and lone pairs eliminates the quinoidal bonding pattern adopted by **P1**. This is apparent from the local aromaticity within central donor and acceptor rings in the n = 8 oligomer of **P2**, which show more aromatic NICS values of –6.09 ppm (ring 34, Table S6) and –6.42 ppm (ring 37, Table S6), respectively. This can be attributed to the delocalization of the lone pair on sulfur within the donor, which affords higher intra-ring aromaticity.[74] More negative NICS values that range between –6 and –7 along the entire π-conjugated backbone of **P2** are consistent with an aromatic bonding pattern (Tables S6 and S11). Thus, **P2** possesses a non-zero diradical index (y = 4.2 × 10^{-4}) only at n = 8 with ΔE_{ST} converging to approximately –4.68 kcal mol^{-1}. This indicates the formation of a low-spin ground state with minimal diradical character in the polymeric long-chain ($n \rightarrow \infty$) limit. These data are consistent with the assignment of the ground electronic state obtained using temperature-dependent EPR and SQUID magnetometry measurements. The relative values of ΔE_{ST} for **P1** and **P2** are consistent with the magnitudes computed here.

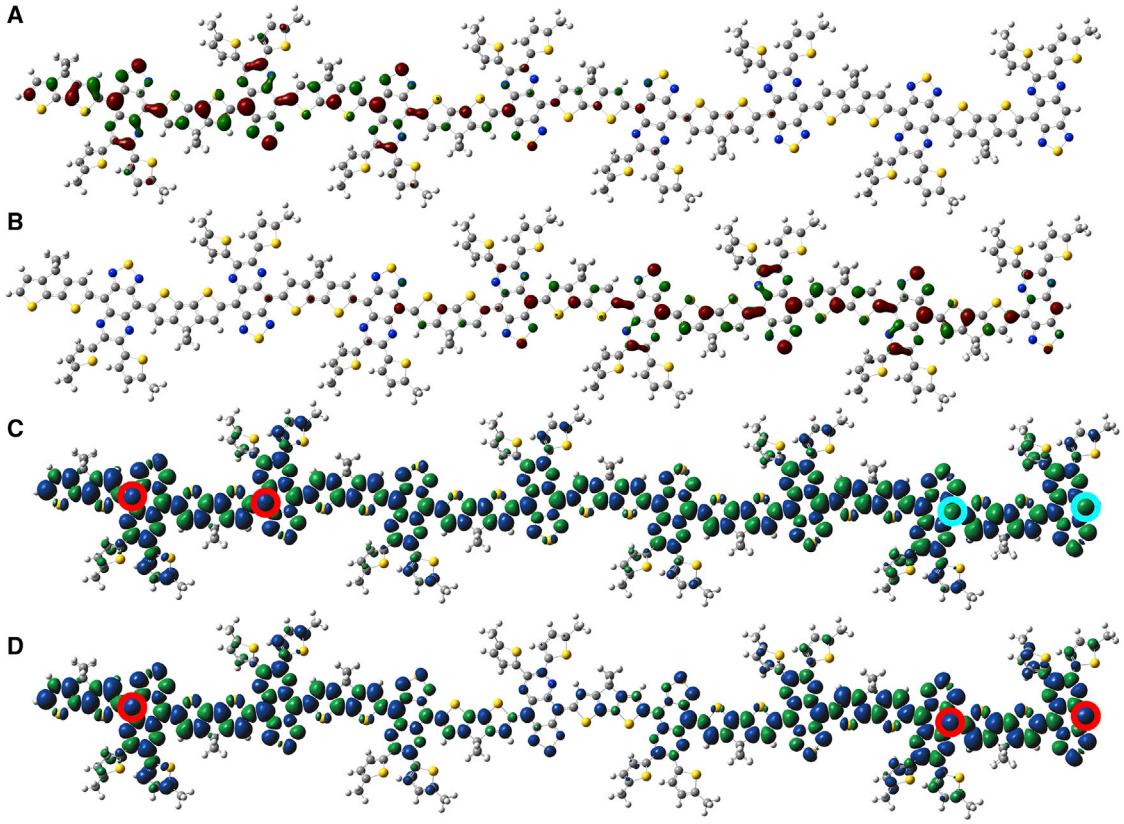

Figure 7. Electronic structure of the P1 oligomer (n = 8) at the UB3LYP/6-31G level of theory**

(A and B) Calculated (A) α-SOMO and (B) β-SOMO profiles of the open-shell singlet.

(C) Spin density distribution of the singlet and (D) triplet states with most probable locations for the unpaired electrons highlighted with open circles (red: up spin; blue: down spin).

For a singlet diradical, one would expect that significant overlap exists between the α- and β-SOMOs, whereas a triplet would minimize overlap and diminish effects associated with DSP. These features are apparent in the topological structures of **P1** and **P2** and illustrated in the evolution of the electronic structure of **P1**, which progresses from a low-spin species with moderate y (0.313 at n = 4) to the bond dissociation limit ($y \rightarrow 1$) at longer chain lengths and then adopts a high-spin ground state. For **P1** and **P2** oligomers ($n < 4$), the frontier MOs show considerable overlap (Figures S11–S14). Evolution and divergence in the electronic and topological structure becomes evident upon increasing the chain length. For the **P1** singlet, an increase from $n = 4 \rightarrow 8$ results in a progressive localization of the α- and β-SOMOs from the quinoidal core to the oligomer periphery (Figures 7A, 7B, S15, S17, and S20). As a result, antiferromagnetically coupled spins occupy separate spaces, which serves to diminish bond covalency, increase y, and mitigate electron repulsion. However, an extension of the conjugation length also leads to enhanced Coulomb repulsion from the spatial overlap of α- and β-SOMOs and a rapid decrease in ΔE_{ST}.

The triplet is stabilized at longer chain lengths since the increased spacing between unpaired electrons further reduces Coulomb repulsion.[73] This is consistent with the more localized spin density of the S = 1 octamer (Figures 7C and 7D) and consistent with the spin-orbit coupling with nitrogen in the 2P ESEEM echo measurements, g-factor of 2.0035, and weak intramolecular ferromagnetic coupling (J = 1.24 cm^{-1}) between spins (Figure 5C).[75] In contrast, **P2** demonstrates extensive

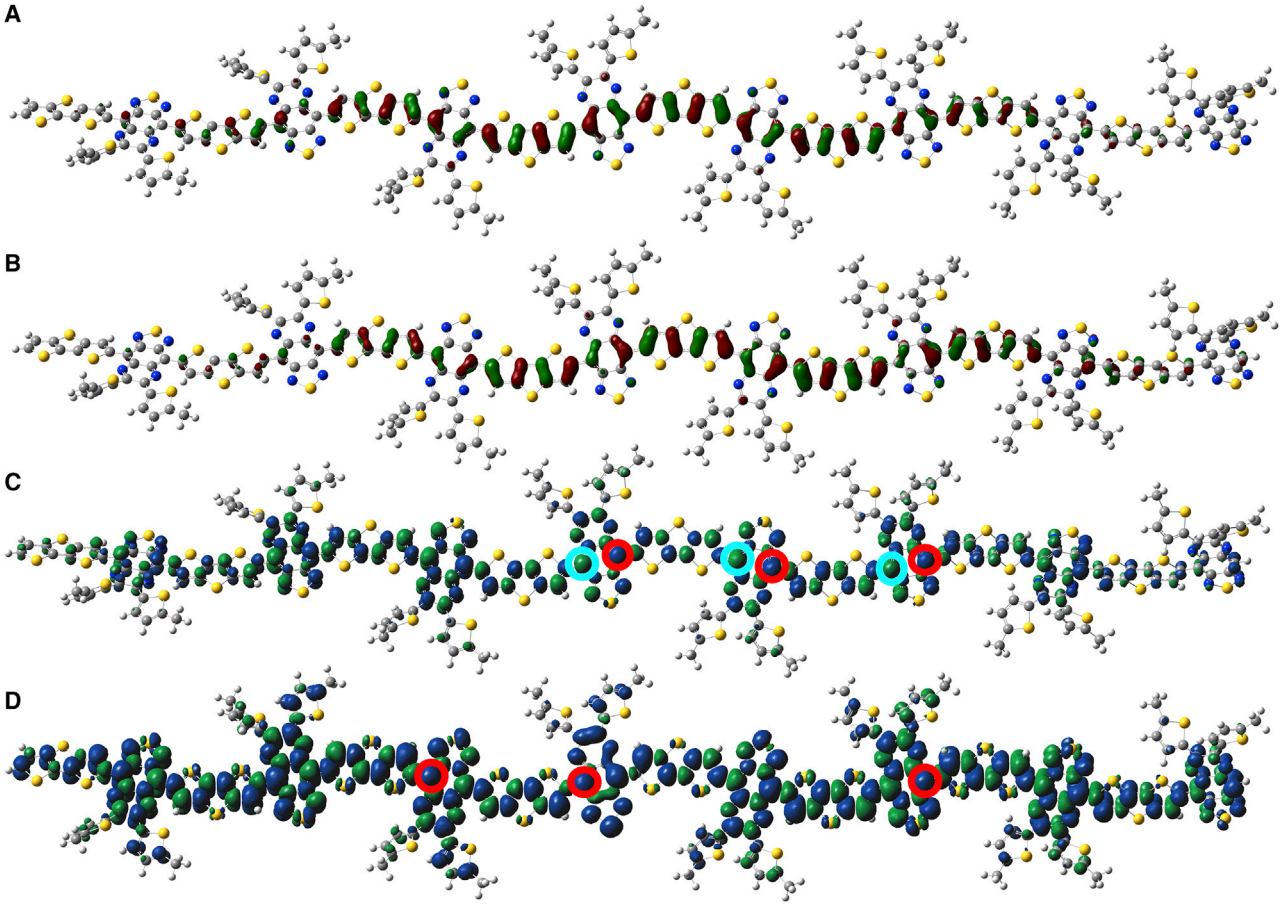

Figure 8. Electronic structure of the P2 oligomer (n = 8) at the UB3LYP/6-31G level of theory**

(A and B) Calculated (A) α-SOMO and (B) β-SOMO profiles of the open-shell singlet.

(C and D) Spin density distribution of the (C) singlet and (D) triplet states with most probable locations for the unpaired electrons highlighted with open circles (red: up spin; blue: down spin).

overlap of α- and β-SOMOs along the backbone in both the singlet and triplet states (Figures 8A–8C). The extensive distribution of spin density is consistent with enhanced DSP, a singlet ground state, and marginal y. The slight shift in g factor for **P2** also follows from similar observations in the computed triplet of the n = 8 oligomer as this would be the species detected in EPR measurements (Figure 8D).

In order to better articulate the chemical and topological evolution of the electronic structure and elaborate on the large differences in properties within the context of strongly correlated π-electron systems, we carried out anisotropy of the induced current density (ACID) calculations on the oligomer series (Figures S24–S29). This describes the global aromaticity and assists in visualizing the pathway followed by delocalized electrons.[76] At n = 2, the ring currents for both **P1** and **P2** indicate diatropic (aromatic) circuits within individual donor and acceptor units (Figure S25) in agreement with NICS calculations. The ring current within the TQ acceptor is largely retained with considerable delocalization into ancillary thiophene rings. For **P1** at n = 4, the paratropic (quinoidal) ring current within the central TQ benzenoid unit and the CPDT donor increases in magnitude, consistent with the concomitant decrease in NICS values (Table S4; Figure S26). Enhanced inter-ring π-delocalization becomes evident between donor and acceptor units in **P1** for n > 4, while the pathway

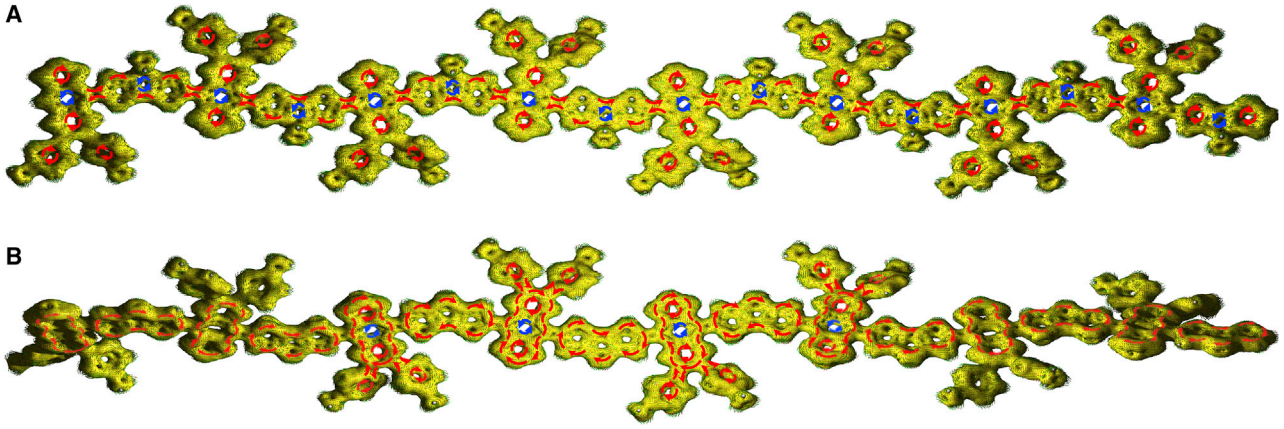

Figure 9. ACID plots of the P1 and P2 oligomers (*n* = 8) at the UB3LYP/6-31G level of theory**

(A and B) Isosurface (yellow) and current density vectors (green lines) calculated by ACID for (A) the open-shell triplet state of **P1** and (B) open-shell singlet state of **P2**. The general aromatic current is indicated by the superimposed clockwise red arrows. The current density vectors plotted on the ACID isosurface indicate ring current (red: clockwise, aromatic; blue: counterclockwise, anti-aromatic) and prevalent delocalization pathways present.

extending to the ancillary thiophenes begins to degrade. While **P2** shows a similar trend, there is more confinement of electron density within the individual DA repeat units as the conjugation length increases. While both **P1** and **P2** demonstrate extensive delocalization along the π-conjugated backbone, the difference between electronic pathways becomes more pronounced at longer chain lengths (Figure 9). For **P1** at *n* = 8, strong paratropic ring currents are evident along the entire backbone, consistent with quinoidal character and NICS calculations (Figure S28; Table S6). In **P1**, paratropic ring currents within the donor core show substantial ordering, while outer diatropic currents are largely disrupted by a lack of a conjugation across the $C(CH_3)_2$ bridgehead (Figure 9A). For **P2**, the bridgehead sulfur enables more flow and ordering of outer diatropic currents along the donor periphery (Figures 9B and S29). While a weak paratropic current in the central benzenoid unit of TQ is evident for **P2**, it is smaller in magnitude than **P1**. Taken collectively, the strong paratropic ring currents in **P1** are consistent with stronger intramolecular DA coupling. This follows the computed bond-length values between the donor and acceptor components where **P1** has connecting bonds varying between 1.40 and 1.44 Å (approaching a C=C bond length), while **P2** varies between 1.44 and 1.45 Å (approaching a C-C bond length) (Table S11). The increased single-bond character between units in **P2** permits increased bond rotation between donor and acceptor components (dihedral angles of 3.20° and 9.93°, respectively) thereby diminishing the co-planarity as evident in Figure 9. These results are in agreement with the more ordered structure of **P1** obtained in GIWAXS measurements.

DISCUSSION

DA CPs with narrow bandgaps and open-shell (diradical) character represent an emerging class of materials whose rich behavior enables new applications. In contrast to previous work on Kékulé and non-Kékulé materials, these copolymers show significant internal charge transfer character between electron-rich and electron-deficient components, extensive delocalization of electron density, long-range π-mediated spin-spin interactions, very narrow bandgaps, and high chemical stability. Atomistic engineering through substitution of sulfur for carbon at the donor bridgehead enables modulation of the local aromaticity within the donor, which in turn enables control of the topological and ground state structure. This is consistent

with a shift from an aromatic low-spin structure with moderate diradical character adopted by **P2** (S = 0, ΔE_{ST} = –5.24 kcal mol^{-1}) to a quinoidal high-spin structure in **P1** (S = 1, ΔE_{ST} = 7.10 × 10^{-3} kcal mol^{-1}). Spectroscopic, transport, GIWAXS, EPR, and SQUID measurements, complemented by quantum chemical calculations, provide clear correlations between the chemical, electronic, structural, and magnetic features of these materials. The dramatic changes resulting from atom-specific substitution demonstrate that adaptation of these properties is predicated on long-range interactions along a linear π-conjugated pathway. Furthermore, these data indicate the capability to form electronic states with varying energetics (ΔE_{ST}), magnitudes of intramolecular electron-electron pairing ($0 < y < 1$), and diradicals ($y = 1$) with controlled spin alignments. This work provides an approach to develop new structure-property relationships associated with the novel electronic and topological structures adopted by DA CPs, control the ground state configuration, tune distance-dependent spin-spin interactions, and articulate the emergence of the novel properties of these materials.

EXPERIMENTAL PROCEDURES

Resource availability

Lead contact

Further information and requests for resources and reagents should be directed to the Lead Contact, Prof. Jason D. Azoulay (jason.azoulay@usm.edu).

Materials availability

Reagents generated in this study will be made available on request, but we may require a payment and/or a completed Materials transfer agreement if there is potential for commercial application.

Data and code availability

All data generated and analyzed during this study are included in this article and its supplemental information.

General procedures

Full descriptions of the synthesis, experimental procedures, data treatment, and computational methods can be found in the Supplemental experimental procedures. In addition, stability studies for the polymers, along with tabulated half-lives of different radical species, are provided in Figures S30–S35 and Table S12, respectively.

SUPPLEMENTAL INFORMATION

Supplemental information can be found online at https://doi.org/10.1016/j.xcrp.2021.100467.

ACKNOWLEDGMENTS

The work performed at The University of Southern Mississippi was made possible through the Air Force Office of Scientific Research (AFOSR) under support provided by the Organic Materials Chemistry Program (grant FA9550-20-1-0353, Program Manager: Dr. Kenneth Caster), the National Science Foundation (OIA-1757220), and US Army Engineer Research and Development Center (ERDC) under PE 0603734A, Project T15, Task "Advanced Polymer Development" under ERDC BAA 18-0500 "Multifunctional Materials to Address Military Engineering" executed under contract no. W912HZ-18-C-0022. DFT calculations were performed at USM using the High Performance Computational (HPC) Cluster supported by the NSF

(OAC-1626217). The EPR measurements at the University of Alabama were supported by the National Science Foundation (CHE-1416238). M.K.B.'s effort in this study was supported by the Russian Ministry of Science and Higher Education within grant 14.W03.31.0034 (megagrant). L.A.G. and X.G. acknowledge support from the US Department of Energy, Office of Science, Office of Basic Energy Sciences under award number DE-SC0019361 for the scattering characterization. K.S.M., L.A.G., and E.R.K. acknowledge traineeship support from the NSF NRT program "Interface" (DGE-1449999) through the University of Southern Mississippi.

AUTHOR CONTRIBUTIONS

J.D.A. conceived the project and oversaw all aspects of the research. K.S.M. and N.E. synthesized the molecules. P.M. and K.S.M. performed DFT calculations. EPR, absorption, conductivity, scattering, SQUID magnetometry, and GPC were performed by M.M.L., L.H., L.A.G., K.S.M., D.J.A., and E.R.K. under the supervision of X.G., M.K.B., and J.D.A. K.S.M., D.J.A., and J.D.A. wrote the manuscript.

DECLARATION OF INTERESTS

L.H., N.E., and J.D.A. are inventors on a patent application filed by the University of Southern Mississippi related to the polymers described in this work.

Received: March 15, 2021
Revised: May 4, 2021
Accepted: May 25, 2021
Published: June 16, 2021

REFERENCES

1. Abe, M. (2013). Diradicals. Chem. Rev. *113*, 7011–7088.
2. Huang, Y., and Egap, E. (2018). Open-shell organic semiconductors: an emerging class of materials with novel properties. Polym. J. *50*, 603–614.
3. Y Gopalakrishna, T., Zeng, W., Lu, X., and Wu, J. (2018). From open-shell singlet diradicaloids to polyradicaloids. Chem. Commun. (Camb.) *54*, 2186–2199.
4. Chen, Z.X., Li, Y., and Huang, F. (2021). Persistent and stable organic radicals: Design, synthesis, and applications. Chem *7*, 288–332.
5. Swager, T.M. (2017). 50th anniversary perspective: Conducting/semiconducting conjugated polymers. A personal perspective on the past and the future. Macromolecules *50*, 4867–4886.
6. Hu, X., Wang, W., Wang, D., and Zheng, Y. (2018). The electronic applications of stable diradicaloids: present and future. J. Mater. Chem. C Mater. Opt. Electron. Devices *6*, 11232–11242.
7. Nakano, M. (2017). Open-shell-character-based molecular design principles: Applications to nonlinear optics and singlet fission. Chem. Rec. *17*, 27–62.
8. Lukman, S., Richter, J.M., Yang, L., Hu, P., Wu, J., Greenham, N.C., and Musser, A.J. (2017). Efficient singlet fission and triplet-pair emission in a family of zethrene diradicaloids. J. Am. Chem. Soc. *139*, 18376–18385.
9. Minami, T., and Nakano, M. (2012). Diradical character view of singlet fission. J. Phys. Chem. Lett. *3*, 145–150.
10. Morita, Y., Nishida, S., Murata, T., Moriguchi, M., Ueda, A., Satoh, M., Arifuku, K., Sato, K., and Takui, T. (2011). Organic tailored batteries materials using stable open-shell molecules with degenerate frontier orbitals. Nat. Mater. *10*, 947–951.
11. Wang, K., Huang, L., Eedugurala, N., Zhang, S., Sabuj, M.A., Rai, N., Gu, X., Azoulay, J.D., and Ng, T.N. (2019). Wide potential window supercapacitors using open-shell donor–acceptor conjugated polymers with stable n-doped states. Adv. Energy Mater. *9*, 1902806.
12. Yuan, D., Guo, Y., Zeng, Y., Fan, Q., Wang, J., Yi, Y., and Zhu, X. (2019). Air-stable n-type thermoelectric materials enabled by organic diradicaloids. Angew. Chem. Int. Ed. Engl. *58*, 4958–4962.
13. Kim, W.Y., and Kim, K.S. (2008). Prediction of very large values of magnetoresistance in a graphene nanoribbon device. Nat. Nanotechnol. *3*, 408–412.
14. Sanvito, S. (2011). Molecular spintronics. Chem. Soc. Rev. *40*, 3336–3355.
15. Lombardi, F., Lodi, A., Ma, J., Liu, J., Slota, M., Narita, A., Myers, W.K., Müllen, K., Feng, X., and Bogani, L. (2019). Quantum units from the topological engineering of molecular graphenoids. Science *366*, 1107–1110.
16. Slota, M., Keerthi, A., Myers, W.K., Tretyakov, E., Baumgarten, M., Ardavan, A., Sadeghi, H., Lambert, C.J., Narita, A., Müllen, K., and Bogani, L. (2018). Magnetic edge states and coherent manipulation of graphene nanoribbons. Nature *557*, 691–695.
17. Rudebusch, G.E., Zafra, J.L., Jorner, K., Fukuda, K., Marshall, J.L., Arrechea-Marcos, I., Espejo, G.L., Ponce Ortiz, R., Gómez-García, C.J., Zakharov, L.N., et al. (2016). Diindeno-fusion of an anthracene as a design strategy for stable organic biradicals. Nat. Chem. *8*, 753–759.
18. Sun, Z., Ye, Q., Chi, C., and Wu, J. (2012). Low band gap polycyclic hydrocarbons: from closed-shell near infrared dyes and semiconductors to open-shell radicals. Chem. Soc. Rev. *41*, 7857–7889.
19. Sun, Z., Zeng, Z., and Wu, J. (2014). Zethrenes, extended p-quinodimethanes, and periacenes with a singlet biradical ground state. Acc. Chem. Res. *47*, 2582–2591.
20. Morita, Y., Suzuki, S., Sato, K., and Takui, T. (2011). Synthetic organic spin chemistry for structurally well-defined open-shell graphene fragments. Nat. Chem. *3*, 197–204.
21. Magda, G.Z., Jin, X., Hagymási, I., Vancsó, P., Osváth, Z., Nemes-Incze, P., Hwang, C., Biró, L.P., and Tapasztó, L. (2014). Room-temperature magnetic order on zigzag edges of narrow graphene nanoribbons. Nature *514*, 608–611.
22. Ruffieux, P., Wang, S., Yang, B., Sánchez-Sánchez, C., Liu, J., Dienel, T., Talirz, L., Shinde, P., Pignedoli, C.A., Passerone, D., et al. (2016). On-surface synthesis of graphene nanoribbons

with zigzag edge topology. Nature *531*, 489–492.

23. Casado, J. (2017). Para-quinodimethanes: A unified review of the quinoidal-versus-aromatic competition and its implications. Top. Curr. Chem. (Cham) *375*, 73.

24. Zeng, Z., Shi, X., Chi, C., López Navarrete, J.T., Casado, J., and Wu, J. (2015). Pro-aromatic and anti-aromatic π-conjugated molecules: an irresistible wish to be diradicals. Chem. Soc. Rev. *44*, 6578–6596.

25. Zeng, W., Phan, H., Herng, T.S., Gopalakrishna, T.Y., Aratani, N., Zeng, Z., Yamada, H., Ding, J., and Wu, J. (2017). Rylene ribbons with unusual diradical character. Chem *2*, 81–92.

26. Ponce Ortiz, R., Casado, J., Hernández, V., López Navarrete, J.T., Viruela, P.M., Ortí, E., Takimiya, K., and Otsubo, T. (2007). On the biradicaloid nature of long quinoidal oligothiophenes: experimental evidence guided by theoretical studies. Angew. Chem. Int. Ed. Engl. *46*, 9057–9061.

27. Casado, J., Ponce Ortiz, R., and López Navarrete, J.T. (2012). Quinoidal oligothiophenes: new properties behind an unconventional electronic structure. Chem. Soc. Rev. *41*, 5672–5686.

28. Dressler, J.J., and Haley, M.M. (2020). Learning how to fine-tune diradical properties by structure refinement. J. Phys. Org. Chem. *33*, e4114.

29. Yui, K., Aso, Y., Otsubo, T., and Ogura, F. (1989). Novel electron acceptors bearing a heteroquinonoid system. I. Synthesis and conductive complexes of 5,5′-bis(dicyanomethylene)-5,5′-dihydro-Δ2,2′-bithiophene and related compounds. Bull. Chem. Soc. Jpn. *62*, 1539–1546.

30. Konishi, A., Hirao, Y., Nakano, M., Shimizu, A., Botek, E., Champagne, B., Shiomi, D., Sato, K., Takui, T., Matsumoto, K., et al. (2010). Synthesis and characterization of teranthene: a singlet biradical polycyclic aromatic hydrocarbon having Kekulé structures. J. Am. Chem. Soc. *132*, 11021–11023.

31. London, A.E., Chen, H., Sabuj, M.A., Tropp, J., Saghayezhian, M., Eedugurala, N., Zhang, B.A., Liu, Y., Gu, X., Wong, B.M., et al. (2019). A high-spin ground-state donor-acceptor conjugated polymer. Sci. Adv. *5*, eaav2336.

32. Yuen, J.D., Wang, M., Fan, J., Sheberla, D., Kemei, M., Banerji, N., Scarongella, M., Valouch, S., Pho, T., Kumar, R., et al. (2015). Importance of unpaired electrons in organic electronics. J. Polym. Sci. A *53*, 287–293.

33. Huang, L., Eedugurala, N., Benasco, A., Zhang, S., Mayer, K.S., Adams, D.J., Fowler, B., Lockart, M.M., Saghayezhian, M., Tahir, H., et al. (2020). Open-shell donor–acceptor conjugated polymers with high electrical conductivity. Adv. Funct. Mater. *30*, 1909805.

34. Li, Y., Li, L., Wu, Y., and Li, Y. (2017). A review on the origin of synthetic metal radical: Singlet open-shell radical ground state? J. Phys. Chem. C *121*, 8579–8588.

35. Yuen, J.D., and Wudl, F. (2013). Strong acceptors in donor–acceptor polymers for high performance thin film transistors. Energy Environ. Sci. *6*, 392–406.

36. Joo, Y., Huang, L., Eedugurala, N., London, A.E., Kumar, A., Wong, B.M., Boudouris, B.W., and Azoulay, J.D. (2018). Thermoelectric performance of an open-shell donor–acceptor conjugated polymer doped with a radical-containing small molecule. Macromolecules *51*, 3886–3894.

37. Salem, L., and Rowland, C. (1972). The electronic properties of diradicals. Angew. Chem. Int. Ed. Engl. *11*, 92–111.

38. Zeng, Z., Ishida, M., Zafra, J.L., Zhu, X., Sung, Y.M., Bao, N., Webster, R.D., Lee, B.S., Li, R.W., Zeng, W., et al. (2013). Pushing extended p-quinodimethanes to the limit: stable tetracyano-oligo(N-annulated perylene) quinodimethanes with tunable ground states. J. Am. Chem. Soc. *135*, 6363–6371.

39. Dressler, J.J., Cárdenas Valdivia, A., Kishi, R., Rudebusch, G.E., Ventura, A.M., Chastain, B.E., Gómez-García, C.J., Zakharov, L.N., Nakano, M., Casado, J., and Haley, M.M. (2020). Diindenoanthracene diradicaloids enable rational, incremental tuning of their singlet-triplet energy gaps. Chem *6*, 1353–1368.

40. Rajca, A. (1994). Organic diradicals and polyradicals: From spin coupling to magnetism? Chem. Rev. *94*, 871–893.

41. Gallagher, N.M., Olankitwanit, A., and Rajca, A. (2015). High-spin organic molecules. J. Org. Chem. *80*, 1291–1298.

42. Rajca, A., Wongsriratanakul, J., and Rajca, S. (2001). Magnetic ordering in an organic polymer. Science *294*, 1503–1505.

43. Lahti, P.M. (1999). Magnetic Properties of Organic Materials (Taylor & Francis).

44. Kumar, S., Kumar, Y., Keshri, S., and Mukhopadhyay, P. (2016). Recent advances in organic radicals and their magnetism. Magnetochemistry *2*, 42.

45. Su, J., Telychko, M., Hu, P., Macam, G., Mutombo, P., Zhang, H., Bao, Y., Cheng, F., Huang, Z.-Q., Qiu, Z., et al. (2019). Atomically precise bottom-up synthesis of π-extended [5] triangulene. Sci. Adv. *5*, eaav7717.

46. Talirz, L., Ruffieux, P., and Fasel, R. (2016). On-surface synthesis of atomically precise graphene nanoribbons. Adv. Mater. *28*, 6222–6231.

47. Clair, S., and de Oteyza, D.G. (2019). Controlling a chemical coupling reaction on a surface: Tools and strategies for on-surface synthesis. Chem. Rev. *119*, 4717–4776.

48. Fujii, S., and Enoki, T. (2013). Nanographene and graphene edges: electronic structure and nanofabrication. Acc. Chem. Res. *46*, 2202–2210.

49. Guo, X., Baumgarten, M., and Müllen, K. (2013). Designing π-conjugated polymers for organic electronics. Prog. Polym. Sci. *38*, 1832–1908.

50. Kim, M., Ryu, S.U., Park, S.A., Choi, K., Kim, T., Chung, D., and Park, T. (2020). Donor–acceptor-conjugated polymer for high-performance organic field-effect transistors: A progress report. Nat. Nanotechnol. *30*, 1904545.

51. Tam, T.L.D., Wu, G., Chien, S.W., Lim, S.F.V., Yang, S.-W., and Xu, J. (2020). High spin pro-quinoid benzo[1,2-c;4,5-c′]bisthiadiazole conjugated polymers for high-performance solution-processable polymer thermoelectrics. ACS Mater. Lett. *2*, 147–152.

52. Ji, X., and Fang, L. (2021). Quinoidal conjugated polymers with open-shell character. Polym. Chem. *12*, 1347–1361.

53. Karafiloglou, P. (1989). The double (or dynamic) spin polarization in π diradicals. J. Chem. Educ. *66*, 816.

54. Salzmann, I., Heimel, G., Oehzelt, M., Winkler, S., and Koch, N. (2016). Molecular Electrical Doping of Organic Semiconductors: Fundamental Mechanisms and Emerging Dopant Design Rules. Acc. Chem. Res. *49*, 370–378.

55. Veciana, J., and Iwamura, H. (2000). Organic magnets. MRS Bull. *25*, 41–51.

56. Yoshizawa, K., and Hoffmann, R. (1995). The role of orbital interactions in determining ferromagnetic coupling in organic molecular assemblies. J. Am. Chem. Soc. *117*, 6921–6926.

57. Blundell, S.J., and Pratt, F.L. (2004). Organic and molecular magnets. J. Phys. Condens. Matter *16*, R771.

58. Gryn'ova, G., Coote, M.L., and Corminboeuf, C. (2015). Theory and practice of uncommon molecular electronic configurations. Wiley Interdiscip. Rev. Comput. Mol. Sci. *5*, 440–459.

59. Wang, R., Ko, C.-H., Brugh, A.M., Bai, Y., Forbes, M.D.E., and Therien, M.J. (2020). Topology, distance, and orbital symmetry effects on electronic spin–spin couplings in rigid molecular systems: Implications for long-distance spin–spin interactions. J. Phys. Chem. A *124*, 7411–7415.

60. Parker, T.C., Patel, D.G., Moudgil, K., Barlow, S., Risko, C., Brédas, J.-L., Reynolds, J.R., and Marder, S.R. (2015). Heteroannulated acceptors based on benzothiadiazole. Mater. Horiz. *2*, 22–36.

61. Li, H., Zhou, F., Tam, T.L.D., Lam, Y.M., Mhaisalkar, S.G., Su, H., and Grimsdale, A.C. (2013). Comparative studies on the electrochemical and optical properties of representative benzo[1,2-c;4,5-c′]bis[1,2,5] thiadiazole, [1,2,5]-thiadiazolo[3,4-g] quinoxaline and pyrazino[2,3-g]quinoxaline derivatives. J. Mater. Chem. C Mater. Opt. Electron. Devices *1*, 1745–1752.

62. Miyaji, T., Tsubota, Y., Suzuki, T., Yamashita, Y., Mukai, T., and Miyashi, T. (1992). Tetracyanoquinodimethanes fused with 1,2,5-thiadiazole and pyrazine units. Heterocycles *33*, 337, 336.

63. Dallos, T., Hamburger, M., and Baumgarten, M. (2011). Thiadiazoloquinoxalines: tuning physical properties through smart synthesis. Org. Lett. *13*, 1936–1939.

64. Yan, P., Xie, A., Wei, M., and Loew, L.M. (2008). Amino(oligo)thiophene-based environmentally sensitive biomembrane chromophores. J. Org. Chem. *73*, 6587–6594.

65. Kini, G.P., Lee, S.K., Shin, W.S., Moon, S.-J., Song, C.E., and Lee, J.-C. (2016). Achieving a solar power conversion efficiency exceeding 9% by modifying the structure of a simple, inexpensive and highly scalable polymer.

J. Mater. Chem. A Mater. Energy Sustain. *4*, 18585–18597.

66. Tsuda, A., and Osuka, A. (2001). Fully conjugated porphyrin tapes with electronic absorption bands that reach into infrared. Science *293*, 79–82.

67. Bleaney, B., and Bowers, K.D. (1952). Anomalous paramagnetism of copper acetate. Proc. R. Soc. Lond. A *214*, 451–465.

68. Cullity, B.D., and Graham, C.D. (2008). Introduction to Magnetic Materials, Second Edition (John Wiley & Sons).

69. Huang, J., and Kertesz, M. (2007). Intermolecular covalent π-π bonding interaction indicated by bond distances, energy bands, and magnetism in biphenalenyl biradicaloid molecular crystal. J. Am. Chem. Soc. *129*, 1634–1643.

70. Mims, W.B. (1972). Envelope modulation in spin-echo experiments. Phys. Rev. B *5*, 2409–2419.

71. Dikanov, S.A., and Tsvetkov, Y. (1992). Electron Spin Echo Envelope Modulation (ESEEM) Spectroscopy (CRC Press).

72. Frisch, M.J., Trucks, G.W., Schlegel, H.B., Scuseria, G.E., Robb, M.A., Cheeseman, J.R., Scalmani, G., Barone, V., Petersson, G.A., Nakatsuji, H., et al. (2016). Gaussian 16 Rev. C.01.

73. Snyder, G.J. (2012). Rational design of high-spin biradicaloids in the isobenzofulvene and isobenzoheptafulvene series. J. Phys. Chem. A *116*, 5272–5291.

74. Dressler, J.J., Teraoka, M., Espejo, G.L., Kishi, R., Takamuku, S., Gómez-García, C.J., Zakharov, L.N., Nakano, M., Casado, J., and Haley, M.M. (2018). Thiophene and its sulfur inhibit indenoindenodibenzothiophene diradicals from low-energy lying thermal triplets. Nat. Chem. *10*, 1134–1140.

75. Schott, S., McNellis, E.R., Nielsen, C.B., Chen, H.Y., Watanabe, S., Tanaka, H., McCulloch, I., Takimiya, K., Sinova, J., and Sirringhaus, H. (2017). Tuning the effective spin-orbit coupling in molecular semiconductors. Nat. Commun. *8*, 15200.

76. Geuenich, D., Hess, K., Köhler, F., and Herges, R. (2005). Anisotropy of the induced current density (ACID), a general method to quantify and visualize electronic delocalization. Chem. Rev. *105*, 3758–3772.